

Chapter 13

INFRARED AIRGLOW

R.D. Sharma

Infrared radiance observed by a detector looking at the earth's undisturbed atmosphere is called infrared airglow. This radiation may arise from rotational transitions, as is the case for radiation from water vapor around $17 \mu\text{m}$, or from electronic transitions, for example, the O_2 ($a^1\Delta_g \rightarrow X^3\Sigma_g^-$) transition causing the airglow at $1.27 \mu\text{m}$ (0-0 band) and at $1.58 \mu\text{m}$ (0-1 band). However, the most common sources of infrared airglow are the vibrational-rotational (V-R) transitions within the ground electronic state. This class of transitions includes emission from OH, CO_2 , O_3 , NO, and H_2O . Figure 13-1 gives the energy level diagram of CO_2 and points out the more commonly encountered transitions. Table 13-1 gives the band origins and Table 13-2 the Einstein A coefficients for some OH V-R bands. For additional information on the energy levels and the radiative lifetimes of the infrared active species see Chapter 12. The extent of the wavelength range covered by the term infrared is not well defined. We will limit this discussion to the spec-

Table 13-1. OH Vibrational Transition Band Origins [L.S. Rothman et al., 1983]

v'	$\Delta v = 1$		$\Delta v = 2$		$\Delta v = 3$	
	(cm^{-1})	(μm)	(cm^{-1})	(μm)	(cm^{-1})	(μm)
1	3570	2.80				
2	3404	2.94	6974	1.43		
3	3240	3.09	6644	1.50	10214	0.98
4	3078	3.25	6318	1.58	9722	1.03
5	2915	3.43	5993	1.67	9233	1.08
6	2752	3.63	5667	1.76	8745	1.14
7	2585	3.87	5337	1.87	8252	1.21
8	2415	4.14	5000	2.00	7752	1.29
9	2237	4.47	4652	2.15	7237	1.38

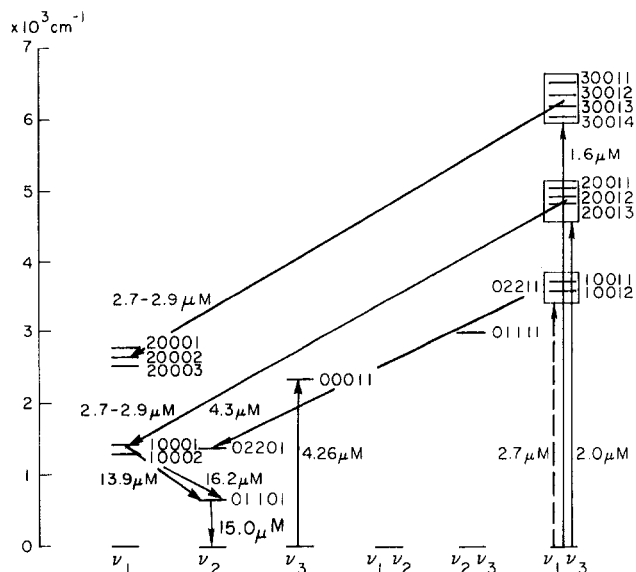


Figure 13-1. The energy levels of carbon dioxide. The lowest levels of bending mode and asymmetric stretch, which lead to transitions at 15.0 and $4.26 \mu\text{m}$, are shown. Also shown are the upper and lower levels for some of the important transitions observed in the infrared airglow of the earth's atmosphere. The notation in the figure is the same as in AFGL line tape [Rothman and Young, 1981]. (Reprinted with permission from Pergamon Press Ltd. © 1981.)

tral region from 1.2 to $17 \mu\text{m}$. This rather arbitrarily restricted wavelength range leaves out several important airglow emissions, including the $63 \mu\text{m}$ emission from oxygen atoms [Offermann and Grossmann, 1978]. This latter process together with the $5.3 \mu\text{m}$ ($1 \rightarrow 0$) emission from NO and the $15 \mu\text{m}$ radiation from the bending mode of CO_2 are the important processes in the cooling of the thermosphere [Craig and Gille, 1969; Kockarts, 1980; Gordiets et al., 1983; Zachor, Sharma, Nadile and Stair, 1981].

Infrared airglow has been the subject of a number of studies [Stair et al., 1981; Gordiets et al., 1978; Ogawa, 1976]. It is a quickly changing field because of the rapidly improving measurement and analysis technology and it is not surprising, therefore, that the information in the literature is a few years behind that available to workers in the field. For this reason, the emphasis in this chapter has been placed upon results obtained at AFGL.

13.1 SOURCES OF THE INFRARED AIRGLOW

13.1.1 Resonant Scattering of the Earthshine

Radiation upwelling through the atmosphere from the surface of the earth is called earthshine. Although the average temperature of the earth's surface is 296 K , the tem-

CHAPTER 13

Table 13-2. Thermally-averaged OH ($X^2 \pi_1$) vibrational Einstein coefficients $A_{V''V'}$ (s^{-1}) for 200 K [Mies, 1974] (Reprinted with permission from Academic Press © 1974)

$V'' =$	0	1	2	3	4	5	6	7	8	9
$V' = 1$	20.15									
2	14.07	25.24								
3	0.92	39.93	20.90							
4	0.079	4.29	72.61	12.25						
5	0.050	0.392	10.62	108.4	4.47					
6		0.053	1.274	20.99	141.5	2.347				
7			0.183	2.907	37.32	163.4	9.142			
8			0.030	0.569	5.67	60.84	166.8	25.84		
9				0.130	1.189	10.81	90.28	146.6	50.65	

perature of the earthshine depends upon altitude and wavelength. For example in the 12-13 μm region, where the absorption due to the earth's atmosphere is minimal, the upwelling radiation can be described by 296 K blackbody radiation independent of altitude. On the other hand, radiation in the 15 μm region up to the lower mesosphere (about 70 km altitude) can be described as radiation from a blackbody with temperature given by the local translational temperature. At higher altitudes, because of the lack of sufficient collisions, the upwelling 15 μm radiation can be described by about 200 K blackbody temperature.

Whatever the variations in the temperature of the earthshine, it is clear that this radiation has appreciable intensity only at longer wavelengths ($\lambda > 5 \mu\text{m}$). It can, therefore, excite only the lower vibrational levels of the infrared active molecules. The excited molecules can reradiate isotropically without change of frequency causing infrared airglow. Resonant scattering of earthshine by the ν_3 mode of ozone is an important contributor to the airglow at 9.6 μm . The 15 μm radiation from the bending mode of carbon dioxide also contains an important contribution from the earthshine.

13.1.2 Scattering of Sunshine

In contrast to the earthshine which populates only the lowest lying vibrational levels, solar radiation (~ 6000 K blackbody temperature) plays an important role in exciting higher vibrational levels corresponding to $\lambda \leq 5 \mu\text{m}$. The vibrational levels thus produced can lose their energy by optical transitions to the ground state (resonant scattering) or by radiation to other lower excited vibrational levels (nonresonant scattering or fluorescence). The effect of sunshine is shown in the dramatic increase in the airglow near 4.3 μm during the day due to scattering by the ν_3 mode of CO_2 [James and Kumer, 1973]. Scattered solar radiation, resonant and nonresonant, also contributes to the CO_2 airglow at 2.7 μm , the important absorption bands being located near 2.7 μm [Kumer, 1981], 2.0, and 1.6 μm [Sharma et al., 1981].

A process capable of producing large amounts of infrared airglow radiation is the electronic excitation of molecules by sunshine followed by emission of a longer wavelength photon. The molecule is thus left in an excited vibrational state, the final vibrational level being determined by the Franck-Condon integrals. Several quanta of infrared photons may be emitted before the molecule relaxes to the ground state. This process, however, has not been identified as the source of any airglow from the quiescent atmosphere.

13.1.3 Photodissociation

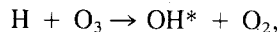
Dissociation of molecular species by solar radiation contributes to the airglow by producing fragments in excited states. An example is the airglow of O_2 ($a^1\Delta_g \rightarrow X^3\Sigma_g^-$) at 1.27 μm (0-0 transition) and at 1.58 μm (0-1 transition). The $\text{O}_2(a^1\Delta_g)$ state is mainly produced by the photodissociation of O_3 by solar ultraviolet radiation around 255 nm.

Photodissociation of molecular species can also modify the infrared airglow due to reduced density of the photodissociating molecules and/or increased density of the product species. Photodissociation of O_3 also leads to reduced daytime airglow of OH not only because of the reduced production of OH by the reaction $\text{H} + \text{O}_3 \rightarrow \text{OH} + \text{O}_2$ but also due to the more rapid $\text{OH} + \text{O} \rightarrow \text{O}_2 + \text{H}$ depletion reaction. The latter reaction becomes faster because of the enhanced oxygen atom concentrations produced by photodissociation of O_3 . The net result is that daytime OH emissions around 1.5 μm ($\Delta v = 2$) and around 3.0 μm ($\Delta v = 1$) are much weaker than their nighttime intensities.

13.1.4 Chemical Reactions

Creation of molecular species in the excited state by chemical reactions and their subsequent decay contributes to airglow. The airglow produced by this mechanism is also called chemiluminescence. A well-known example of this process is the OH radiation around 1.5 and 3.0 μm and at

shorter wavelengths, even visible regions, OH being produced by the chemical reaction



the asterisk denoting the vibrational excitation. Another example of this process [Stair et al., 1981, 1985] is the radiation around 9.6 μm from the ν_3 mode of O_3 produced by the three body recombination reaction



13.1.5 Atomic and Molecular Collisions

Collisions of infrared radiating species with other molecules lead to transfer of vibrational energy from one collision partner to the other. This transfer is much more efficient if the vibrational frequencies of the transitions involved are not too far apart (near-resonant), that is $\omega\tau \sim 1$, where ω is the frequency separation between the transitions involved and τ the time duration of the collision. Because of the near-resonance, N_2 transfers its vibrational energy efficiently to the ν_3 mode of CO_2 [Sharma and Brau, 1969]. This energy transfer process plays an important role in the enhanced nighttime 4.3 μm airglow of CO_2 around 70 km [Kumer et al., 1978].

Another important type of collision producing infrared airglow is that in which the relative translational energy of atom-molecule or molecule-molecule is converted into vibrational excitation of the molecule. These collisions lead to establishment of local thermodynamic equilibrium (LTE) between various degrees of freedom, the only requirement being that enough of these take place during the effective radiative lifetime of the emitter (taking into account self-absorption). Even when the frequency of collisions is not sufficient to establish LTE, this type of collision may be an important source of vibrational excitation. Examples are collisions above 90 km of oxygen atoms with CO_2 and NO which play a very important role in the airglow at 15 μm and 5.3 μm , respectively [Degges, 1971; Zachor et al., 1981; Sharma and Nadile, 1981].

Another important source of vibrational energy is the collisional excitation of molecules by electronically excited atoms. For example, oxygen atoms produced by photodissociation of O_3 are created in the excited ^1D state with unit efficiency. These atoms are very efficiently quenched by molecular nitrogen. During the quenching process, a fraction of the electronic excitation of oxygen atoms is converted into vibrational energy of N_2 [McEwan and Phillips, 1975] and can be collisionally transferred to CO_2 and emitted as 4.3 μm airglow.

The processes described in the above sections are the most important but by no means the only sources of infrared radiation from the undisturbed atmosphere. Raman scattering of the solar radiation is a less important source of airglow

because of the very small cross sections involved. In addition, there is Rayleigh scattering of solar radiation important only below about 40 km altitude.

13.2 NON-LOCAL THERMODYNAMIC EQUILIBRIUM (NLTE)

We note again that except for 1.27 μm and 1.58 μm $\text{O}_2(a^1\Delta_g \rightarrow X^3\Sigma_g^-)$ radiation the infrared airglow from 1.2 to 15 μm involves molecular vibrational-rotational transitions. In the lower part of the atmosphere (below about 40 km altitude) these vibrational transitions can generally be described by local thermodynamic equilibrium (LTE), that is, vibrational excitation of the molecules can be described by a Boltzmann distribution with a vibrational temperature equaling the translational temperature. Even at these altitudes the $\text{O}_2(a^1\Delta_g)$ electronically excited state population cannot be described by a distribution with a temperature equaling the translational temperature and is much larger than predicted on the basis of LTE. The reason for this lies in the metastable nature of the $\text{O}_2(a^1\Delta_g)$ state (its radiative lifetime is about 65 min) and small rates of collisional quenching by major atmospheric species [McEwan and Phillips, 1975]. This metastable nature and the fact that collisions are not a rapid process for depopulating this state, account for the great abundance of $\text{O}_2(a^1\Delta_g)$ in the stratosphere and mesosphere.

At higher altitudes (starting about 70 km) the vibrational population of the radiating species, even those that are not metastable and are neither produced by chemical reaction nor pumped by sunshine or earthshine, becomes different from what would be predicted on the basis of LTE. Situations deviating from LTE behavior are called NLTE cases. Sometimes it is useful to introduce the concept of vibrational temperature. The concept is based on the fact that near-resonant vibration-to-vibration transfer processes are much faster than nonresonant vibration-to-translation processes. The time needed for the vibrational energy to be partitioned according to a Boltzmann distribution in a collision between identical molecules is usually several orders of magnitude shorter than the time needed to establish LTE in gases [Sharma, 1969; Taylor, 1974]. The vibrational temperature T_v is defined by the relation

$$\ln \left(\frac{g_e n_1}{g_l n_e} \right) = \frac{C_2 E}{T_v}$$

where n_e and n_1 are the excited state and low state number densities, g_e and g_l are the respective statistical weights, $C_2 = 1.4399 \text{ K/cm}^{-1}$ is the second radiation constant and E is the energy difference between the upper and lower states in cm^{-1} .

The concept of vibrational temperature has been used to calculate [Sharma and Nadile, 1981] the contribution to

CHAPTER 13

the 15 μm radiation by the transition $02201 \rightarrow 01101$ of CO_2 . Only when this contribution is added to that of the $01101 \rightarrow 00001$ transition from all the isotopes is a reasonable agreement obtained between the 15 μm radiation observed by the rocket experiment SPIRE in the 70 and 90 km tangent height and the calculated CO_2 radiances [Stair et al., 1981, 1985].

The concept of vibrational temperature cannot be used in all NLTE situations. For example, the vibrational population of OH around 80 km altitude cannot be described by a Boltzmann distribution. This concept, however, is used where possible because it also gives an idea of the extent of deviation from LTE.

It should be pointed out that while fewer collisions lead to NLTE situations, more frequent collisions do not guarantee LTE behavior. This is illustrated by the 2.7 μm daytime CO_2 emission that can still be characterized around 50 km altitude by vibrational temperature about 100 K higher than the translational temperature. This emission, in part, is shown to arise from the absorption of sunlight at 1.5 μm by very weak $00001 \rightarrow 3001$ ($x = 1,2,3$) bands (Figure 13-1) [Sharma et al., 1981]. Although each absorbed photon has a rather small probability of being emitted in the 2.7 μm region, the large number of absorbed photons yields a detectable signal.

Having stated the differences between LTE and NLTE situations in some detail, we will focus for the remainder of this discussion on NLTE airglows, specifically 1–18 μm emissions originating from altitudes higher than 40 km. The LTE situation has been discussed in great detail by other workers [see, for example, Clough et al., 1981].

13.3 METHODS OF MEASUREMENT

Infrared airglow has been studied with rockets [Stair et al., 1974; Nadile et al., 1977; Stair et al., 1981; Markov, 1969; Offermann and Grossmann, 1978] and satellites [Markov et al., 1976]. In this chapter the primary emphasis will be, for reasons cited earlier, on the work at AFGL. Many of the AFGL rockets were launched from Poker Flats, Alaska [Stair et al., 1975]. The rocket payloads contained either limb-viewing or zenith-viewing light collecting and analyzing instruments. In these experiments the instrument package included a protective cover that was opened at a specified altitude during the free ballistic flight phase. The altitude for cover opening, determined by the requirement that the infrared emission due to shock heating by the rocket be sufficiently small, was 50 km or higher.

The simplest infrared sounding rockets measure the infrared radiance reaching the payload from the atmosphere above it. If the payload is not provided with an attitude control system, the rocket usually cones around an axis that makes a small angle with the vertical direction. When measuring the infrared fluorescence, care is taken that the sun is never directly in the line-of-sight (LOS). As the rocket

gains altitude, less and less of the gas is being looked at so that the signal during ascent usually decreases with time (except during atmospheric disturbances); during the descent the reverse is true. However, both in ascent and descent, the magnitude of the derivative of the signal with altitude is a measure of the local radiance—provided we are dealing with an optically thin and steady state one-dimensional atmosphere. Figure 13-2 shows a typical spectral profile of

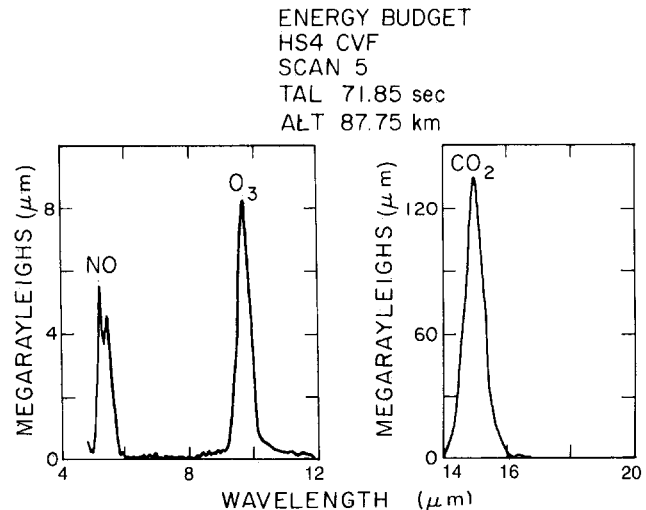


Figure 13-2. Plot of radiance vs wavelength from the zenith looking CVF "Energy Budget" rocket at 87.75 km altitude. The signal from CO_2 at 15 μm is at least an order of magnitude larger than that from NO at 5.3 μm or ozone at 9.6 μm .

zenith emission from the NO vibrational-rotational (V-R) fundamental transition ($\Delta v = 1$) at 5.3 μm , the $001 \rightarrow 000$ V-R band of O_3 at 9.6 μm , and the $01101 \rightarrow 00001$ band of CO_2 at 15 μm obtained by a rocket launched from Andoya, Norway during the Energy Budget Campaign [Ulwick et al., 1983]. This rocket was launched in November 1980 at 0314 UT. Since the solar shadow height was 400 km above the launch site, the experiment was essentially conducted in a night atmosphere.

Another approach useful for viewing weak infrared atmospheric emissions is to add a telescope to the optical system and observe the infrared radiation from the earth-limb. The telescope with a small fraction of degree full viewing angle (usually about 1/4 degree) and excellent off-axis rejection keeps the footprint of the LOS a few kilometers wide. The limb-looking SPIRE (SPectral Infrared Rocket Experiment) has obtained very useful results yielding many new insights into the infrared airglow [Nadile et al., 1977; Stair et al., 1981]. In the SPIRE experiment with the rocket in the exosphere, the earthlimb was scanned vertically through a telescoped circularly variable filter (CVF) spectrometer. The resolution of the instrument was 3% to 4% depending on the wavelength. The tangent height (the distance of closest approach to the earth's surface) is varied

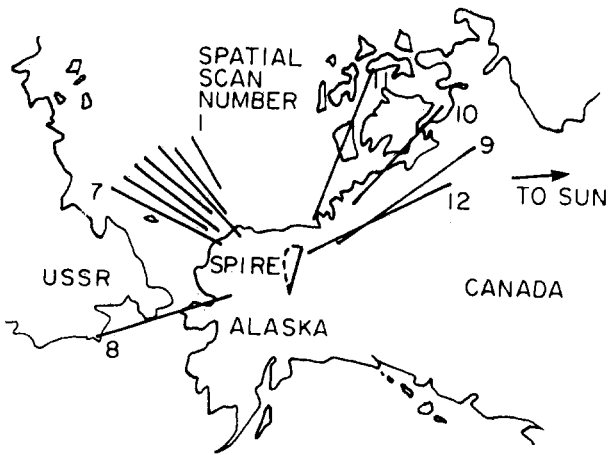


Figure 13-3. Geographical location of projection on earth's surface of tangent heights for various SPIRE scans. Tangent height increases going outwards from the center of figure. Farthest tangent point is 1500 km away from launch site.

by changing the telescope zenith angle. As the tangent height is varied, the location of the LOS and the tangent point (point closest to the earth's surface) also change (Figure 13-3). One result of this spatial scanning is the ability to obtain a day, twilight or night LOS (Figure 13-4). This is in contrast to the zenith-looking rocket where in ascent or descent the region sampled is less than 100 km over the surface of the earth. While the possibility of investigating day-night variations in a zenith-looking experiment is rather limited, it does offer the possibilities of determining the morphology on a small scale.

There are numerous other differences between the zenith

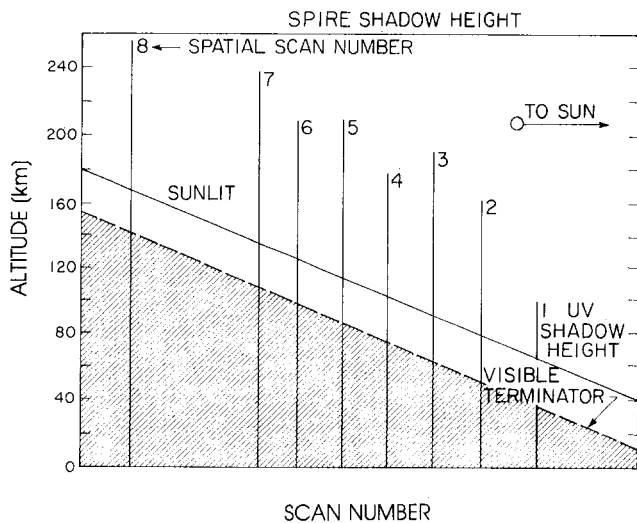


Figure 13-4. Plot showing visible ultraviolet terminators for eight of twelve SPIRE scans. Ultraviolet shadow height is 23 km higher than visible shadow height due to thickness of ozone layer. Scans 9-12 are completely sunlit.

and limb experiments. Two important ones are the amount of the gas sampled and the altitude dependence of the volume probed. In the zenith looking experiment, the length of the LOS between any 1 km altitude interval is $\sec \theta$ km, where θ is the zenith angle of the LOS as long as $\theta \leq 75^\circ$ so that the curvature of the earth is not important. The total volume of the gas sampled is relatively small. Moreover, the zenith experiment weights equal increments of altitude in the LOS equally. Such is not the case in a limb experiment. For example, a detector positioned at an altitude of 285 km looking at 100 km tangent height gathers photons from a path length in excess of 3000 km. Further, for density decreasing monotonically with altitude the volume of the gas sampled drops sharply as we move away from the tangent height. The length of the gas column with altitude between 100 and 101 km is about 227 km. The length of the path sampled with each km increase in altitude decreases in proportion to $[\sqrt{n} - \sqrt{(n-1)}]$ where n and $(n-1)$ are the upper and lower altitudes in km measured from the tangent height. In the example cited above, the length of the LOS between 110 and 111 km is 0.154 times that between 100 and 101 km. Thus, equal increments of altitude in the LOS are not equally weighted in the limb experiment and the radiation from tangent height usually predominates. The above remarks are valid only for an optically thin gas.

A further characteristic of the limb experiment is that because the volume of the gas sampled is so large, the local variations in the atmospheric structure are averaged out. On the other hand, the large column sampled also permits the limb experiment to see some emissions missed by the zenith experiment when performed at the same sensitivity. For example, Figures 13-5 and 13-6 show $15 \mu\text{m}$ radiance from ν_2 band of CO_2 seen by the SPIRE and Energy Budget rockets as a function of altitude. It can be seen in Figure 13-5 that between 95 and 110 km tangent height the band

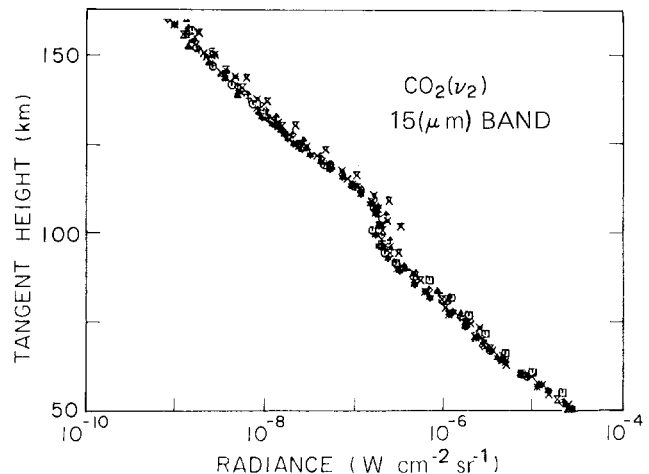


Figure 13-5. Integrated radiance observed by SPIRE in the 14-16 μm interval as function of tangent height. Night scan 8 has 30% higher radiance above 100 km.

CHAPTER 13

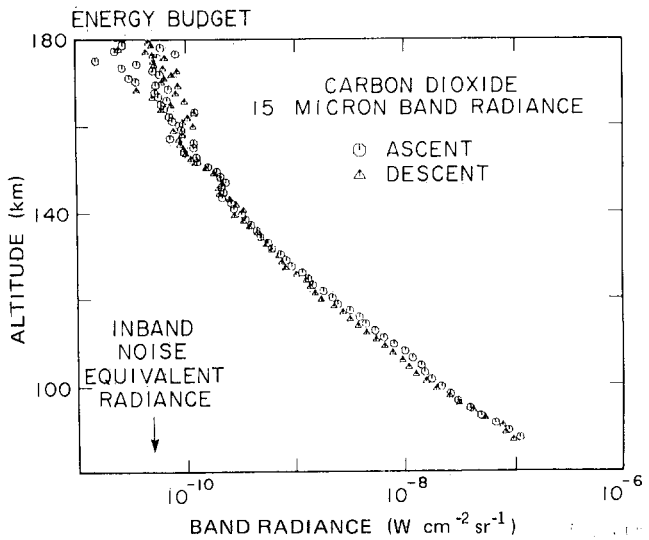


Figure 13-6. Integrated band radiance around 15 μm observed by zenith-looking Energy Budget rocket during ascent and descent as function of altitude.

radiance stays constant although the CO_2 concentration decreases in this altitude range by a factor of 30 to 40. Detailed modeling has shown this phenomenon to be due to oxygen atoms, which are much more efficient at collisionally pumping the CO_2 (01101) level than N_2 or O_2 [Sharma and Nadile, 1981]. The zenith experiment (Figure 13-6) does not give any hint of this behavior in the measured radiances.

Finally, the tangent height in the earthlimb experiment can be varied from zero (earth's surface) to 250 km, whereas the range of altitudes attainable in the zenith experiment is more limited. The two types of experiments emphasize different aspects of infrared airglow and each have their own advantages and disadvantages.

13.4 RESULTS AND DISCUSSION

In this section we introduce the prominent features of the measured airglow and compare them with model calculations. Because of the nature and scope of this chapter, we omit the details of the calculations and approach the subject as an introduction to infrared airglow from the undisturbed atmosphere. Where possible, the published work is referenced; however, a great deal of work is available so far only in the form of non-refereed reports and unpublished work.

We will use SPIRE to illustrate the broad features of the data. SPIRE was launched on September 28, 1977 [Nadile et al., 1977; Stair et al., 1981, 1983]. This payload had three coaligned primary sensors: (1) a telescoped two-channel photometer, (2) a cryogenic (77 K) telescoped short wavelength infrared (SWIR) CVF spectrometer, and (3) a cryogenic (10 K) telescoped long wavelength infrared (LWIR) CVF spectrometer. The spectrometers were coaligned and

covered the 1.4 to 16 μm region. The telescopes had $1/4^\circ$ fields of view with high off-axis rejection (point source rejection of 10^{-5} at 1° off-axis) and were coaligned to better than 0.1° . The payload reached an altitude of 285 km, and the earthlimb was spatially scanned from hard earth to local horizontal at 0.5 deg/s while taking spectra at 2 scans/s. The spectrometers were built at Utah State University and the telescopes at the Honeywell Radiation Center. With a $1/4^\circ$ field of view, the footprint of the LOS varied from 4 to 8 km, depending upon the tangent height and the payload altitude.

Before we give the profiles of the emitted band radiance as a function of tangent height (for the limb-looking experiment) or altitude (for the zenith-looking experiment), we would like to discuss airglow in general terms as a function of altitude. For this purpose we would like to divide the atmosphere above 40 km into several regions. This division is created to facilitate discussion of the SPIRE data. Taking into account the fact that it was an experiment of about 5 min duration at dawn, it is quite possible that the boundaries of the regions created here may have to be modified in context of other data bases. Still we believe it is a useful exercise to point out underlying sources common to the airglow from different bands.

13.4.1 Thermosphere (above 100 km)

This region is characterized by a rapid increase of temperature with altitude. Important emitters in this region are restricted to NO and CO_2 . The airglow, at 5.3 and 15 μm , in this region can be explained primarily in terms of oxygen atom collisions with the emitters. The oxygen atom concentration in this region shows no diurnal variation. The result is that infrared radiation from the excited states produced during the collision of the radiating species with the

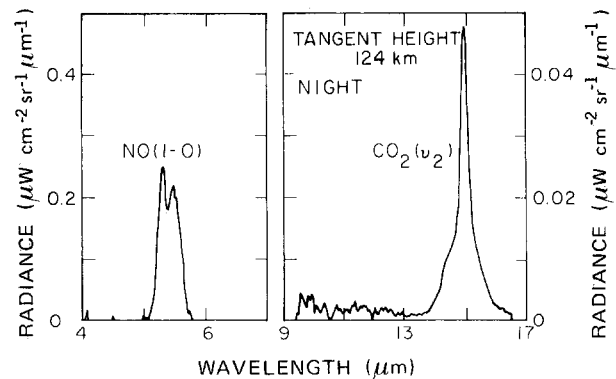


Figure 13-7. Nighttime radiance seen by the long wavelength SPIRE spectrometer as function of wavelength at 124 km tangent height. NO ($1 \rightarrow 0$) band at 5.3 μm and CO_2 ($01101 \rightarrow 00001$) band at 15 μm are the only reproducible spectra seen. Scale for the NO band is 10 times larger than that for CO_2 band. (Daytime results were essentially the same.)

oxygen atoms shows no diurnal variation. A spectrum obtained with the SPIRE liquid-helium-cooled spectrometer at 124 km tangent height is shown in Figure 13-7. Although this spectrum is obtained at night, the post-dawn results are essentially the same. Emission from the 1-0 vibrational band of NO and the 15 μm (01101 \rightarrow 00001) bending mode of CO₂ are the only two features seen at this altitude. Detailed modeling of these emissions indicates that (1) the emissions originate from the NLTE atmosphere with molecular vibrational temperatures lower than the local translational temperatures, (2) the dominant mechanism for vibrational pumping is the collisional excitation by oxygen atoms, and (3) radiative cooling due to NO emissions is the most important atmospheric cooling mechanism (\sim 500 K/day) at these altitudes.

13.4.2 Lower Thermosphere (between 100 km and 85 km)

In this region the oxygen atom concentration begins to decrease without showing any diurnal variation while the temperature shows little change. In this region infrared airglow is characterized by the effect of the solar radiation and oxygen atoms on the radiating species. In addition to the NO and CO₂ bands mentioned above, we see emission from ozone at 9.6 μm (ν_3 band) and the 4.26 μm ν_3 band of CO₂ (Figures 13-8 and 13-9). Because of the large absorption coefficient of 00011 \rightarrow 00001 transition at 4.26 μm , this transition is severely self-absorbed. The ν_3 photons reaching the detector most likely originate from the transition between hot bands and have slightly longer wavelength (around 4.3 μm). The diurnal airglow variations also begin to manifest themselves in the 9.6 μm emission from ozone. At about

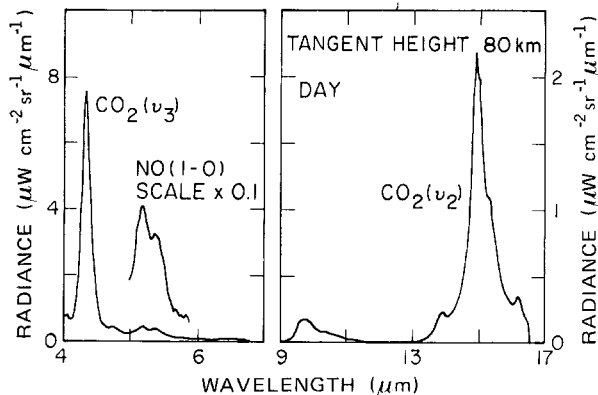


Figure 13-8. Daytime signal from the long wavelength SPIRE spectrometer as function of wavelength at tangent height of 80 km. The 15 μm CO₂ and 5.3 μm NO signals are about the same as in Figure 13-9 (nighttime). The 4.3 μm CO₂ signal is enhanced and 9.6 μm O₃ signal is reduced over nighttime values (Figure 13-9).

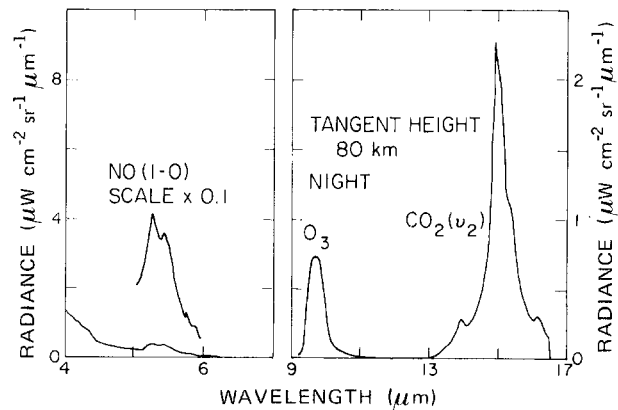


Figure 13-9. Nighttime signal for long wavelength SPIRE spectrometer as function of wavelength at tangent height of 80 km. Notice appearance of O₃ (ν_3) signal. The apparent signal in the 4–6 μm region is due to dielectric relaxation response of the detector to the 15 μm radiation. The 5–6 μm region has been magnified 10-fold to highlight the NO spectral features.

100 km tangent height at night, the ν_3 transition of O₃ begins to appear in the spectrum between 9 and 11 μm (Figure 13-10). At a slightly lower tangent height, this transition appears during the dawn observations as well. While the 001-000 transition of ozone is centered around 9.6 μm , the profile of the emitted radiation appears, in addition, to consist of some hot-band transitions. These transitions are not unambiguously identified as yet and are referred to in the following discussion as the long-wavelength tail of the

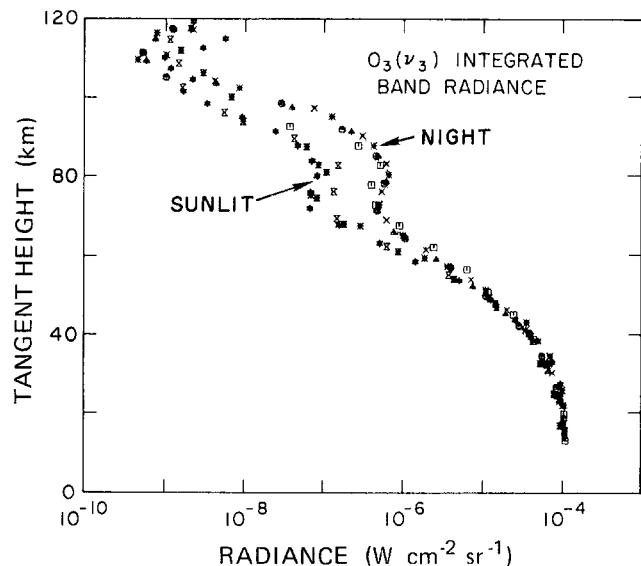


Figure 13-10. 9.6 μm (ν_3) ozone (19.20–10.50 μm) band radiance as function of tangent height. Note stronger nighttime radiance and peak around 80 km. A terminator crossing is evident in scan 1 (\square) where the radiation decreases by an order of magnitude from 85 to 90 km.

CHAPTER 13

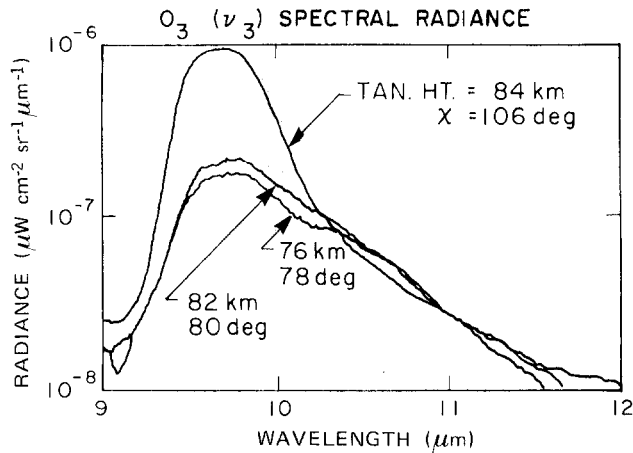


Figure 13-11. 9.6 μm (ν_3) ozone spectrum at 80 km tangent height for different solar elevation angles. The signal for wavelengths longer than 10.2 μm shows no diurnal variation..

9.6 μm emission. The night and day long wavelength tails are essentially the same (Figure 13-11) even though the total O_3 emission decreases dramatically in the daytime. This appears quite reasonable since the day and night oxygen atom concentrations at these altitudes are the same and the vibrationally excited O_3 formed by the $\text{O} + \text{O}_2 + \text{M} \rightarrow \text{O}_3^* + \text{M}$ reaction is the suggested source of the long wavelength ν_3 photon emission. The peak at 9.6 μm results mainly from resonant scattering of earthshine by the ν_3 mode of O_3 and is a measure of O_3 concentration; the smaller daytime value of this scattered radiation reflects the lower daytime O_3 concentration due to photodissocia-

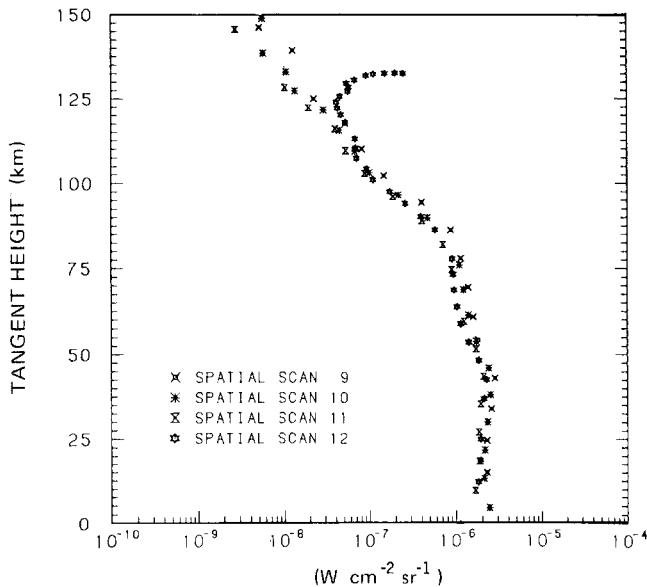


Figure 13-12. Daytime integrated 4.3 μm band radiance observed by short wavelength SPIRE spectrometer as function of tangent height. Larger signal in scan 12 is due to the fact that a deliberate effort was made in this last scan to test the telescope.

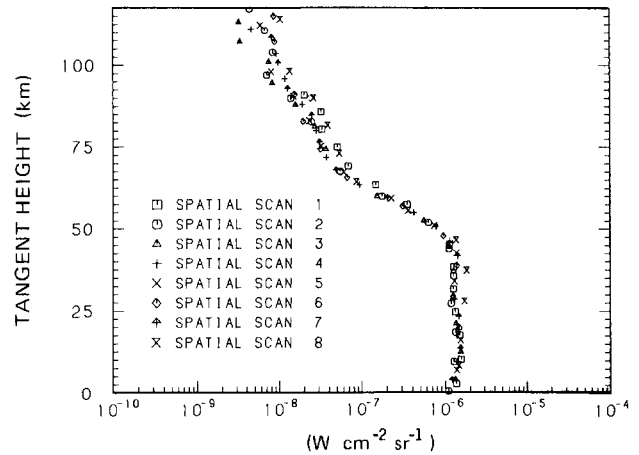


Figure 13-13. Nighttime integrated 4.3 μm band radiance observed by short wavelength SPIRE spectrometer. Notice much faster decrease of the signal above 70 km tangent height than for the daytime case.

tion. The CO_2 4.3 μm ν_3 band daytime radiance seen clearly in Figure 13-12 is over ten times more intense during the day than during the night (Figure 13-13) in agreement with the earlier theoretical prediction of James and Kumer [1973]. As pointed out earlier, the daytime 4.3 μm signal is due to resonance fluorescence as well as nonresonant fluorescence excited by a shorter wavelength, for example, solar radiation (2.7 μm). Near the top of this layer, the collisions of oxygen atoms with CO_2 and NO also play an important role in 15 and 5.3 μm emissions.

13.4.3 Upper Mesosphere (between 85 km and 70 km)

Infrared airglow is primarily determined by processes involving solar radiation during the day (Figure 13-14) and the airglow reaction, $\text{H} + \text{O}_3 \rightarrow \text{OH} + \text{O}_2$ and $\text{HO}_2 + \text{O} \rightarrow \text{OH} + \text{O}_2$ during the night (Figure 13-15). Large

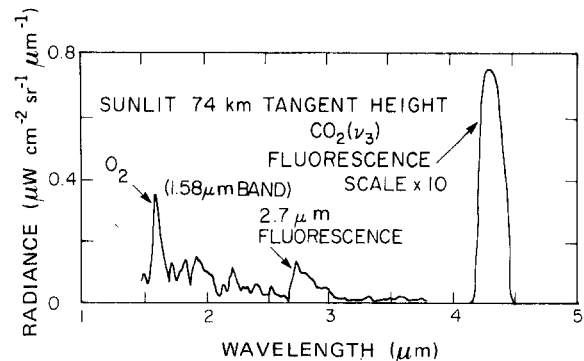


Figure 13-14. The daytime signal from near infrared spectrometer at 74 km tangent height. The nighttime OH radiation is reduced. $\text{O}_2(a\Delta_g, v=0) \rightarrow {}^3\Sigma_g^-(v=1)$ radiation appears at 1.58 μm . The 2.7 μm radiation is fluorescence signal from $\text{CO}_2(\nu_1 + \nu_3$ combination bands) and $\text{H}_2\text{O}(\nu_1$ and ν_3 bands).

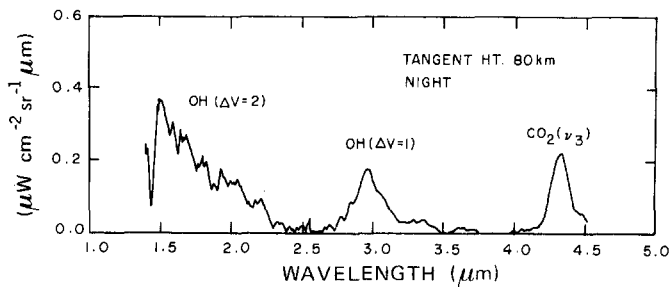


Figure 13-15. The nighttime signal from near infrared spectrometer as function of wavelength. Notice the progression of OH overtone bands ($\Delta v = 2$) between 1.5–2.4 μm and the OH fundamental bands ($\Delta v = 1$) peaked at about 3 μm . The fluorescent emission at 4.3 μm is shown here without the effects of the dielectric relaxation problem encountered in the long wavelength spectrometer.

diurnal differences in the density of oxygen atoms are present. Collisions of the radiating species with oxygen atoms become an unimportant mechanism for depopulating the radiating states because of the small oxygen atom concentration even in daytime. The collisions of the radiating species with N_2 are believed important for OH and CO_2 airglows at night [Kumer et al., 1978].

At a tangent height of about 80 km, the emission around 4.3 μm from CO_2 emission is about 30 times stronger during the day than at night due to absorption of solar radiation (Figures 13-12 and 13-13). Nighttime 4.26 μm fluorescence is primarily due to energy transfer from vibrationally excited N_2 [Kumer et al., 1978], in turn produced by energy transfer from vibrationally hot OH produced by chemical reactions, for example, $\text{H} + \text{O}_3 \rightarrow \text{OH} + \text{O}_2$.

In contrast to the strong daytime emission from CO_2 around 4.3 μm , a strong night-time airglow is seen from OH (Figure 13-15). This airglow is composed of many vibration-rotation bands extending over a wide spectral region from visible to 4 μm . Fundamental vibration-rotation bands ($\Delta v = 1$) and first overtone ($\Delta v = 2$) bands are observed in the infrared [Murphy, 1971] and are shown in Figure 13-11. The overtone hydroxyl emission is broad and appears to be a composite of several vibrational transitions. The fundamental ($\Delta v = 1$) band is less broad and is peaked around 2.9 μm indicating strong contributions from 1-0 and 2-1 vibrational transitions (Table 13-1). It should be pointed out that the Einstein A coefficients for OH overtone emission are larger than those for OH fundamental emission for all upper vibrational levels except $v = 2$ (Table 13-2). The observations cited above appear reasonable if the collisional deactivation rates are closer to the larger of the two sets of Einstein A coefficients. The daytime hydroxyl (Figure 13-14) emissions appear weak. The 1.6 μm region is dominated by $\text{O}_2(a^1\Delta_g)$ emission and the 2.7 μm region by CO_2 and H_2O emission below 70 km.

The emission around 15 μm continues to show no diurnal variations (Figure 13-15). Also, emission at 13.8 and 16.2 μm in the wings of CO_2 15 μm band is observed

(Figures 13-8 and 13-9). This emission is due to the transition from 10001 and 10002 levels to the 01101 level of CO_2 ; the transition from the third level, that is, the 02201 \rightarrow 01101 transition at 668.3 cm^{-1} (compared to 667.3 cm^{-1} for the 01 1 0 \rightarrow 000 transition) makes a substantial contribution to the band radiance but is not resolved from the 01101 \rightarrow 00001 emission. Also not separated are the trace isotope emissions from that of the main isotope. Modeling studies indicate that the contribution of the trace isotopes to the radiance at 15 μm is much larger than expected on grounds of abundance because of the fact that the emission from the 01 1 0 \rightarrow 000 transition of the main isotope is self absorbed at tangent height below 110 km.

Around 80 km, the rates for collisional relaxation of ozone, $\text{O}_3(001) + \text{M} \rightarrow \text{O}_3(000) + \text{M}$, become comparable to the Einstein A coefficient for the radiative relaxation. Rates of collisional relaxation from higher vibrational levels of ozone are not known. A clear description of the underlying processes, therefore, cannot be formulated.

Around 75 km tangent height, the daytime scans show the $a^1\Delta_g \rightarrow X^3\Sigma_g^-$ (0-1) O_2 transition at 1.58 μm ; the 0-0 band of the same electronic transition at 1.27 μm is outside the range of detection and, therefore, not observed. No signal at 1.58 μm is observed at night. The metastable a state has a radiative lifetime of 3.88×10^3 s. The Franck-Condon integral for the 0-1 transition is 0.0131 times that of the 0-0 transition, making the Einstein coefficient of the 0-1 transition about $1.76 \times 10^{-6} \text{ s}^{-1}$ [Krupenie, 1972]. That a finite signal is observed is due to the large length over which light is collected and the large densities of $\text{O}_2(a^1\Delta_g)$ (about $5 \times 10^9 \text{ cm}^{-3}$). Total ground state O_2 density at 74 km is $1.7 \times 10^{14}/\text{cc}$ and that in vibrational level 1 of the ground electronic state is about $3 \times 10^9 \text{ cm}^{-3}$. We thus see that at 74 km tangent height there is complete optical inversion between the $a(v = 0)$ and $X(v = 1)$ states. The gain in the electronic transition is about 10^{-8} per km and assuming a path length of 10^3 km we get signal amplifications of $e^{-0.0001}$. Although the laser action on this transition does not appear likely, the signal shows a large amount of energy stored [$\text{O}_2(a^1\Delta_g) \rightarrow \text{O}_2(X^3\Sigma_g^-)$, 0-1]. The lack of 1.58 μm emission at night indicates that the main source of $\text{O}_2(a^1\Delta_g)$ for the region of the atmosphere discussed here is the photodissociation of O_3 .

13.4.4 Lower Mesosphere (between 70 km and 40 km)

Solar radiation in the strong absorption bands starts becoming depleted as the sunlight traverses this region. Infrared airglow in this region is therefore very dependent on the LOS and three-dimensional atmospheric calculations are needed to model the radiance in this region. Figure 13-16 shows the 0-1 band radiance of the electronic transition ($a^1\Sigma_g \rightarrow X^3\Sigma_g^-$) of O_2 as a function of tangent height. It is seen that the larger the solar elevation angle, the greater the

CHAPTER 13

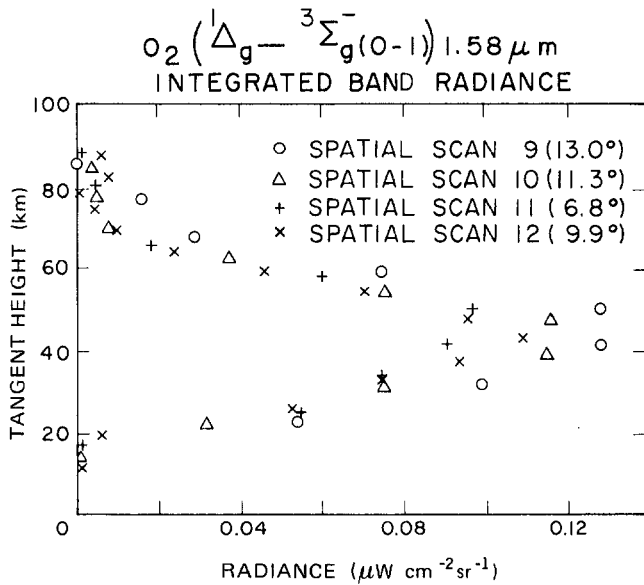


Figure 13-16. Integrated (1.51–1.65 μm) O_2 ($^1\Delta_g$) radiance at 1.58 μm as function of solar elevation angle. Peak signal around 40 km shows inverse correlation with solar elevation (χ) angle.

1.58 μm radiance. Also in contrast to the higher altitudes where nighttime 9.6 μm ν_3 radiance from ozone is larger than the daytime value, the diurnal variation vanishes in the lower part of this altitude range (below about 50 km).

We again point out that this division of the atmosphere into four parts for the discussion of the airglow is rather arbitrary and with a different data base the boundaries between the regions may have to be slightly shifted. However we believe that basic qualitative features of infrared airglow are well described by this division. This method of presenting the data also stresses the common sources that give rise to airglow in different bands and species.

13.4.5 Infrared Radiators

We now present a brief discussion of the airglow classified according to the radiating species in order to summarize the previous discussion as well as to bring out several new points.

13.4.5.1 CO_2 . The CO_2 radiation is seen in the limb-scanning SPIRE experiment at wavelengths of 15, 4.3, and 2.7 μm . 15 μm radiation (Figure 13-5) shows no diurnal variation and is excited mainly by collisions with oxygen atoms above 90 km. Below 90 km altitude the main mechanisms of excitation are the collisions with N_2 and O_2 with the earthshine also playing a role. Above 70 km the 15 μm vibrational temperature lags behind the translational temperature, whereas below 70 km LTE forms a good basis for describing the 15 μm radiation (Figure 13-17).

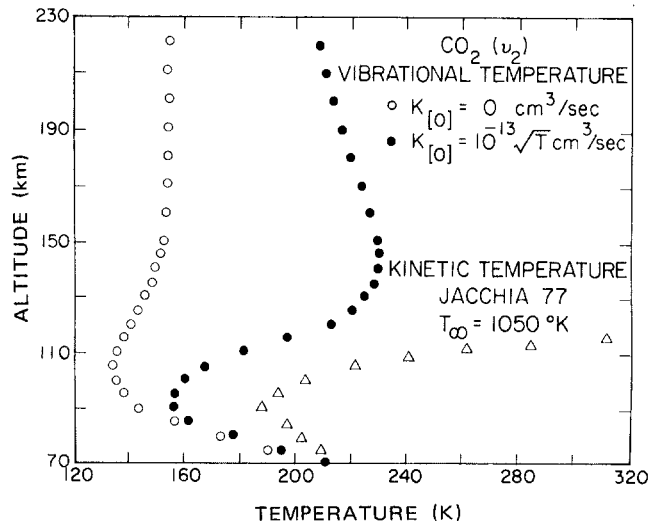


Figure 13-17. Vibrational temperature of bending mode of CO_2 for two rate constants for the deactivation by oxygen above. Kinetic temperature is denoted by triangles.

Solar radiation plays an important role in the fundamental ($\Delta v = 1$) emission from the ν_3 mode at 4.3 μm . Figure 13-18 gives a plot of the vibrational temperature and kinetic temperatures [Degges and Smith, 1977] as functions of altitude. Figures 13-12 and 13-13 give a plot of the 4.3 μm emission observed by SPIRE as a function of tangent height during day and night, respectively. The daytime ra-

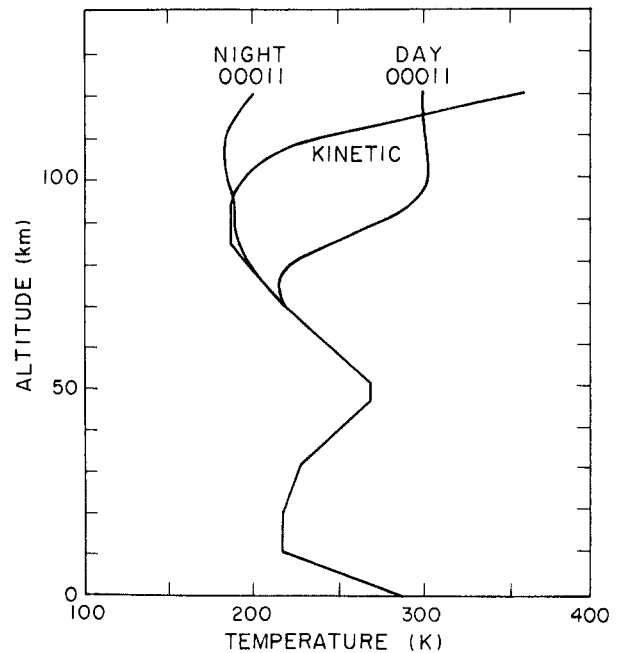


Figure 13-18. Daytime and nighttime vibrational temperatures of asymmetric stretch of CO_2 as function of altitude. Kinetic temperature is also plotted for comparison [Degges and Smith, 1977].

INFRARED AIRGLOW

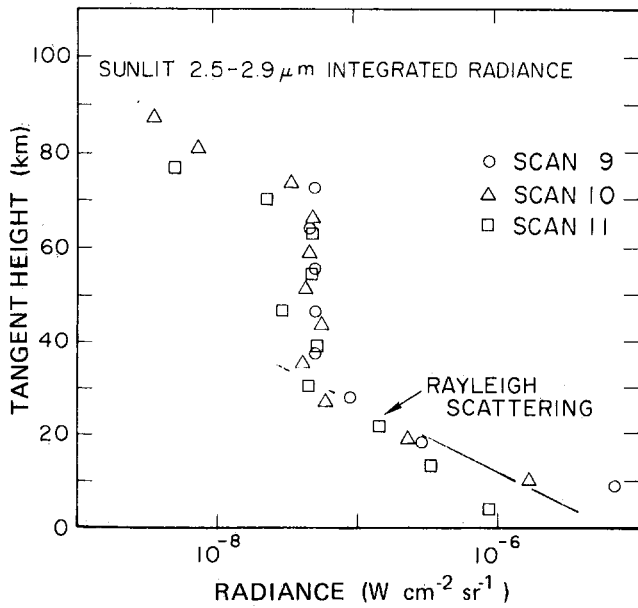


Figure 13-19. Daytime integrated 2.5–2.9 μm band CO_2 and H_2O radiance as function of tangent height. Signal below 30 km is due to Rayleigh scattering.

diance at around 80 km tangent height is about a factor of 30 larger than in nighttime value. Also, Scan 12 was programmed to look almost at the sun at higher altitude. The increased signal around 125 km tangent height is due to telescope leakage.

Radiation at 2.7 μm (Figure 13-19) is observed from CO_2 during daytime only. In addition to CO_2 , there is contribution from H_2O in this band [Kumer, 1981; Sharma et al., 1981].

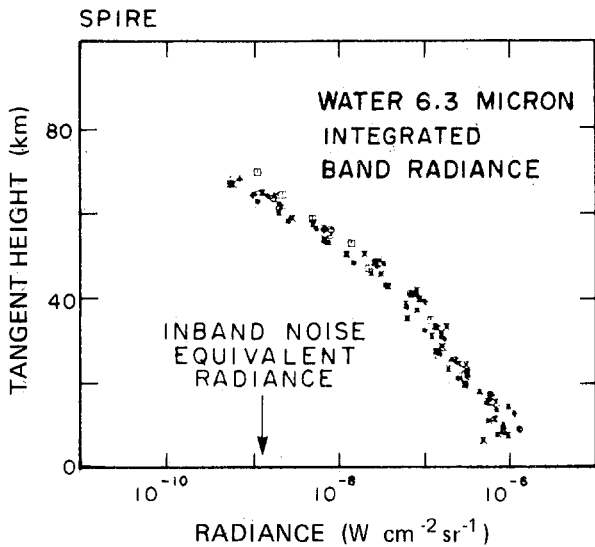


Figure 13-20. 6.3 μm (ν_2) water band radiance (integrated 5.50–6.74 μm) as function of tangent height.

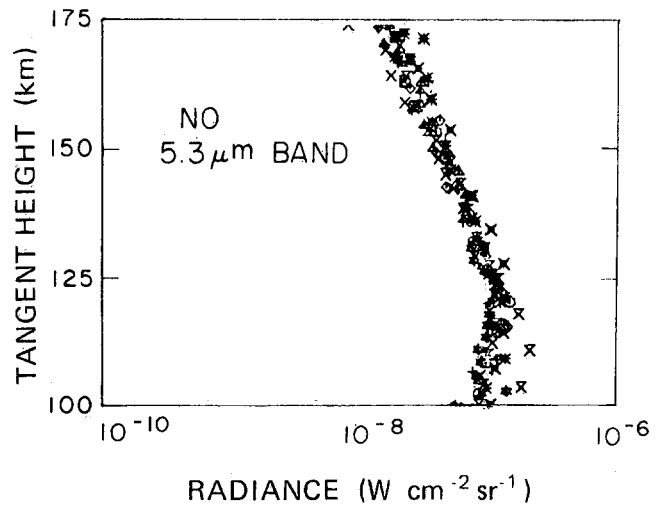


Figure 13-21. Integrated 5.00–5.70 μm NO band radiance as function of tangent height. Night scan 8 gives systematically larger signals around 100 km.

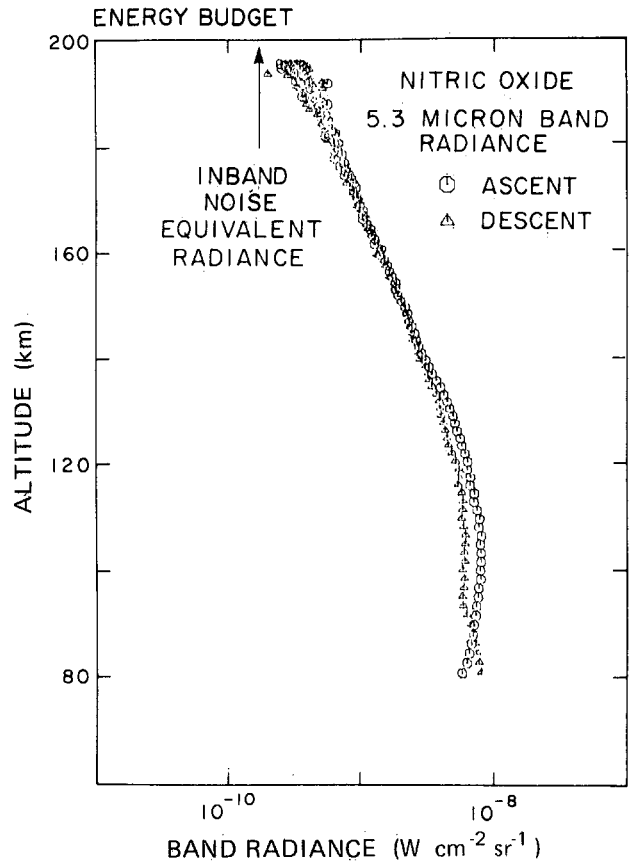


Figure 13-22. Integrated band radiance for the 5.3 μm NO signal observed in the Energy Budget campaign during ascent and descent as a function of tangent height.

CHAPTER 13

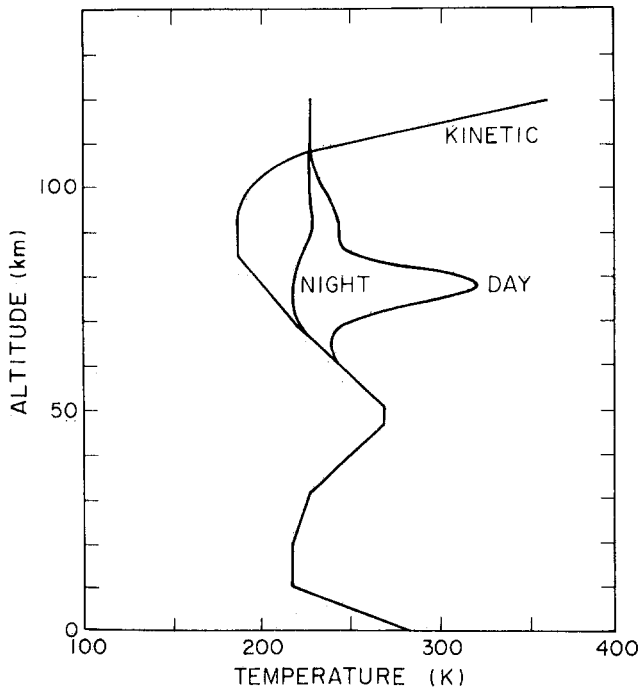


Figure 13-23. Daytime and nighttime vibrational temperatures of ν_3 mode of ozone as function of altitude [Degges and Smith, 1977].

13.4.5.2 H₂O. Radiation from H₂O is observed at 6.3 μm (ν_2 bending mode) and during the daytime around 2.7 μm (ν_1 and ν_3 modes). The radiation at 6.3 μm as a function of tangent height is shown in Figure 13-20. The LOWTRAN 4 radiance model [Selby et al., 1978] using 5 ppm H₂O adequately represents the data between 60 and 70 km tangent heights. Above 70 km the daytime 2.7 μm emission is partly explained at 1.5 ppm of water in a non-LTE model by Degges (private communication, 1984).

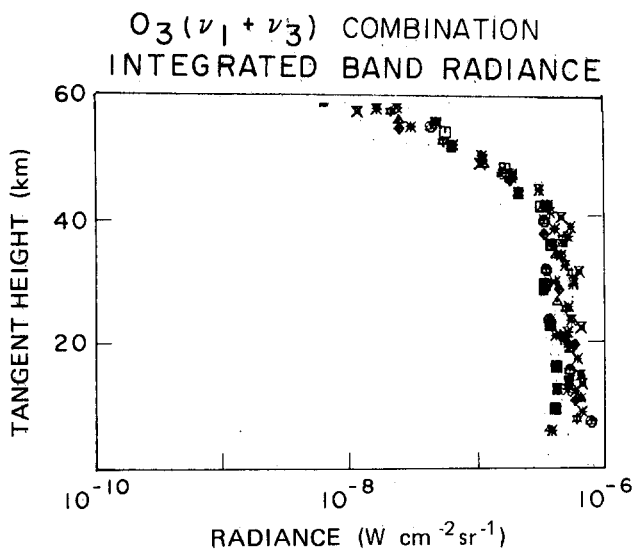


Figure 13-24. 4.8 μm ($\nu_1 + \nu_3$) combination band signal for ozone.

13.4.5.3 NO. The 5.3 μm radiation from NO in the SPIRE data (Figure 13-21) shows no diurnal valuation. Figure 13-22 shows NO radiation from the Energy Budget zenith-looking rocket as a function of altitude. Above 90 km, the oxygen atoms play a dominant role in the 5.3 μm radiation process because of the large rate constant [Degges, 1971; Fernando and Smith, 1979] for the collisional excitation of NO. The 5.3 μm radiation from NO is the major cooling mechanism above 100 km [Kockarts, 1980; Zachor et al., 1981].

13.4.5.4 O₃. Ozone emission is observed around 9.6 μm (ν_3 band) and around 4.8 μm ($\nu_1 + \nu_3$ combination band). Ozone emission at 9.6 μm has been one of the better studied

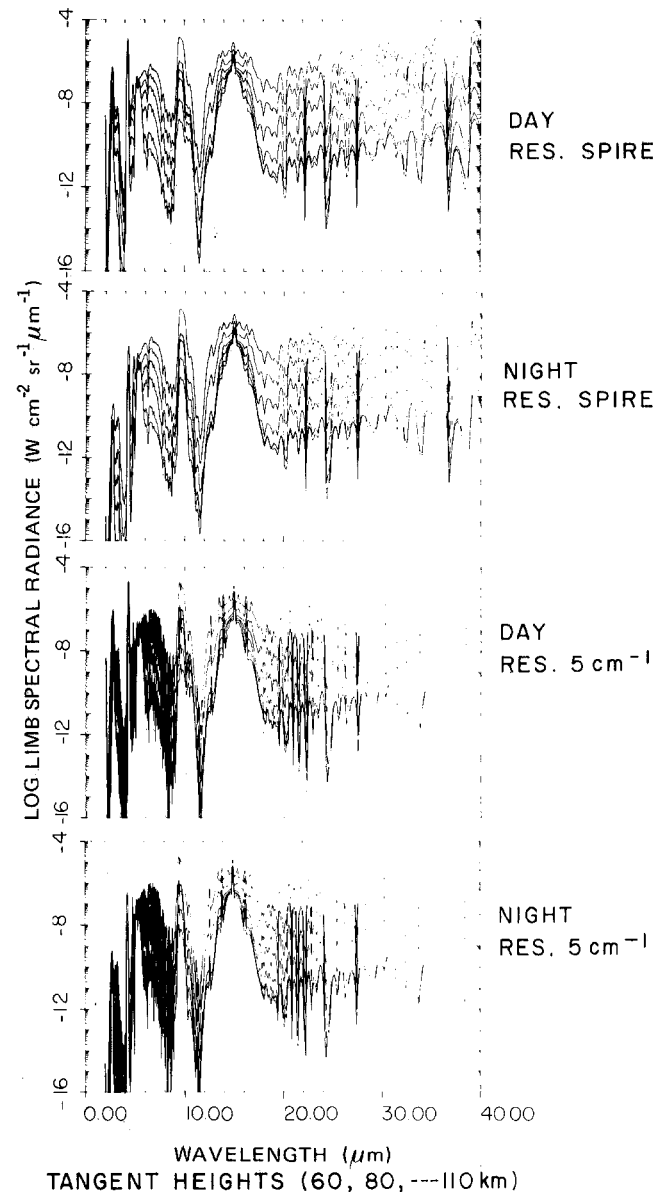


Figure 13-25. Day and night signals predicted using model calculations of T. Degges at SPIRE and 5 cm^{-1} resolutions.

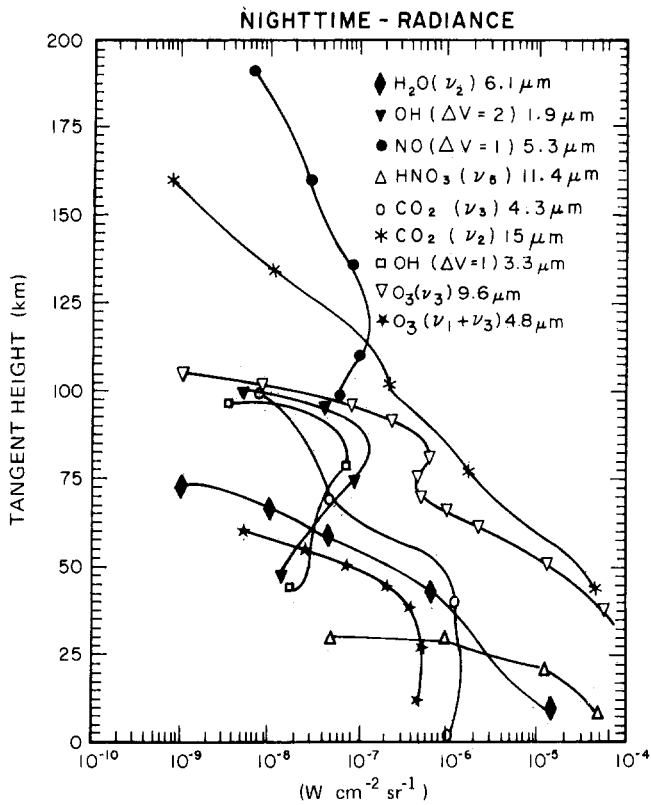


Figure 13-26. Summary of the nighttime signals observed by SPIRE.

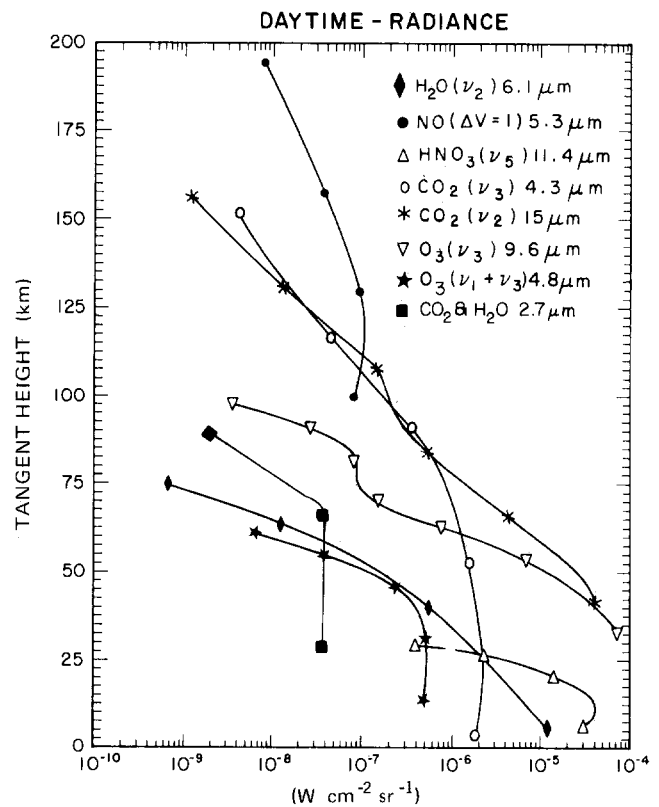


Figure 13-27. Summary of the daytime signals observed by SPIRE.

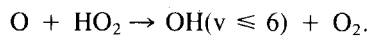
infrared airglow processes [Rawlins et al., 1981]. Figure 13-23 shows the ν_3 vibrational temperature [Degges and Smith, 1977] as a function of altitude. Figures 13-10 and 13-24 show the radiance from the 9.6 and 4.8 μm bands as functions of tangent height.

13.4.5.5 $\text{O}_2(^1\Delta_g)$. The 0-1 band emission at 1.58 μm has been already described in detail. Most of the earlier rocket work has studied the 0-0 emission [Paulsen et al., 1972]. The conclusion of the studies is that the concentration of $\text{O}_2(^1\Delta_g)$ in the atmosphere is $10^9 - 10^{11} \text{ cm}^{-3}$ depending on the altitude.

13.4.5.6 OH. The hydroxyl airglow emission occurs over a relatively narrow altitude region of the mesosphere [Baker et al., 1977]. The peak emission occurs around 85 km and the thickness of the emitting layer is about 10 km. The origin of the hydroxyl emission is believed to be chemiluminescence from two chemical reactions,



and



The model for hydroxyl emission is complex and involves a set of several aeronomic reactions of ozone in an atmosphere containing hydrogen (Moreels et al., 1977).

In addition to the principal radiators mentioned above, there are several minor radiators in the altitude range covered in this article, for example, NO_2 , N_2O and CH_4 .

Figure 13-25 gives a summary of the emission in the 2-40 μm regions as computed by the AFGL Limb Model [Degges and Smith, 1977] at the resolution of the SPIRE experiment ($\Delta\lambda \sim 0.04\lambda$). Principal features discussed above are seen, that is, enhanced daytime emission at 2.7 and 4.3 μm , enhanced nighttime emission at 9.6 μm , as well as diurnally independent emission at 5.3 and 15 μm , and long wavelengths. Also clearly seen is the region (11 to 13 μm) characterized by the absence of infrared airglow. Figures 13-26 and 13-27 give a summary of the nighttime and daytime radiances observed by SPIRE. At high altitudes, NO (5.3 μm) is the most intense emission observed while at low altitudes CO_2 (15 μm) and O_3 (9.6 μm) are the dominant radiators. It should be noted that in the absence of a data base in the 17-40 μm , the radiances in Figure 13-25 can be regarded as theoretical predictions. In the light of future work these predictions may have to be modified.

CHAPTER 13

REFERENCES

- Baker, D.J., T. Conley, and A.T. Stair, "On the Altitude of OH Airglow," (Abstract), *Eos Trans. AGU*, **58**: 460, 1977.
- Clough, S.A., F.X. Kneizys, L.S. Rothman, and W.O. Gallery, "Atmospheric Spectral Transmittance and Radiance: FASCODE1B," *SPIE*, **277**: 152-166, 1981.
- Craig, R.A., and J.C. Gille, "Cooling of the Thermosphere by Atomic Oxygen," *J. Atmos. Sci.*, **26**: 205-209, 1969.
- Degges, T.C., "Vibrationally Excited Nitric Oxide in the Upper Atmosphere," *Appl. Opt.*, **10**: 1856, 1971.
- Degges, T.C. and H.J.P. Smith, "A High Altitude Infrared Radiance Model," AFCRL-TR-77-0271, ADA059242, 1977.
- Fernando, R.P. and I.W.M. Smith, "Vibrational Relaxation of NO by Atomic Oxygen," *Chem. Phys. Lett.*, **66**: 218, 1979.
- Gordiets, B.F., Y.N. Kulikov, M.N. Markov, and M.Ya. Marov, "The Influence of Radiative Cooling and Turbulence on the Heat Budget of the Thermosphere," (To be published in *J. Geophys. Res.*).
- Gordiets, B.F., M.N. Markov, and L.A. Shelpen, "IR Radiation of the Upper Atmosphere," *Planet. Space Sci.*, **26**: 933-948, 1978.
- James, T.C. and J.B. Kumer, "Fluorescence of CO₂ near 4.3 μm: Application to Daytime Limb Radiance Calculations," *J. Geophys. Res.*, **78**: 8320-8329, 1973.
- Kockarts, G., "Nitric Oxide Cooling in the Terrestrial Thermosphere," *Geophys. Res. Lett.*, **7**: 137, 1980.
- Krupenie, P.H., "Spectrum of Molecular Oxygen," *J. Phys. Chem. Ref. Data*, **1**: 423-534, 1972.
- Kumer, J.B., "Analysis of Non-LTE CO₂ SPIRE Earthlimb Data," AIAA Reprint 81-0425, Aerospace Sciences Meeting, Jan 1981.
- Kumer, J.B., A.T. Stair Jr., N. Wheeler, K.D. Baker, and D.J. Baker, "Evidence for an OH⁺ → N₂⁺ → CO₂⁺ → CO₂ + hv(4.3 μm) Mechanism for 4.3 μm Airglow," *J. Geophys. Res.*, **83**: 4743-4747, 1978.
- Markov, M.N., "Molecular Radiation of the Upper Atmosphere in the 3-8 μm Spectral Region," *Appl. Opt.*, **8**: 887, 1969.
- Markov, M.N., G.M. Grechko, A.A. Gubarev, Yu.S. Ivanov, and V.S. Petrov, "Infrared Spectrum of Nitric Oxide Obtained in the Upper Atmosphere at Middle Latitudes by the Orbiting Scientific Station Salyut 4," *Cosmic Res.*, **15**: 102, 1977.
- McClatchey, R.A., W.S. Benedict, S.A. Clough, D.E. Burch, R.E. Calfee, K. Fox, L.S. Rothman, and J.S. Garing, "AFCRL Atmospheric Absorption Line Parameters Compilation," AFCRL-T-73-0096, AD762904, 1973.
- McEwan, M.J. and L.F. Phillips, *Chemistry of the Atmosphere*, The rate constants cited in the book for the deactivation of O₂(¹Δ_g) state by N₂, O₂ and O are ≤ 3 × 10⁻²¹, 2 × 10⁻¹⁸ and ≤ 3 × 10⁻¹⁶ cm molecule⁻¹s⁻¹, respectively, Wiley, New York, p. 140, 1975.
- Mies, F.M., "Calculated Vibrational Transition Probabilities of OH (χ²π)," *J. Mol. Spec.*, **53**: 150, 1974.
- Moreels, G., G. Megie, A. Vallance Jones, and R.L. Gattinger, "An Oxygen-Hydrogen Atmospheric Model and Its Application to the OH Emission Problem," *J. Atmos. Terr. Phys.*, **39**: 551, 1977.
- Murphy, R.E., "Infrared emission of OH in the Fundamental and First Overtone Bands," *J. Chem. Phys.*, **54**: 4852-4859, 1971.
- Nadile, R.M., N.B. Wheeler, A.T. Stair Jr., D.C. Frodsham, and L.C. Wyatt, "SPIRE-Spectral Infrared Experiment" *SPIE*, **24**: 18-24, 1977.
- Offerman, D., and K.V. Grossman, "Spectrometric Measurement of Atomic Oxygen 63 μm Emission in the Thermosphere," *Geophys. Res. Lett.*, **5**: 387, 1978.
- Ogawa, T., "Excitation Processes of Infrared Atmospheric Emissions," *Planet. Space Sci.*, **24**: 749-756, 1976.
- Paulsen, D.E., R.E. Huffman, and J.C. Larabee, "Improved Photoionization Rates of O₂(¹Δ_g) in the D Region," *Radio Sci.*, **7**: 51, 1972.
- Rawlins, W.T., G.E. Caledonia, and J.P. Kennealy, "Observation of Spectrally Resolved Infrared Chemiluminescence from Vibrationally Excited O₃(ν₃)," *J. Geophys. Res.*, **86**: 5297, 1981.
- Rothman, L.S. and L.D.G. Young, "Infrared Energy Levels and Intensities of Carbon Dioxide," *J. Quant. Spectrosc. Radiat. Transfer*, **25**: 505-524, 1981.
- Rothman, L.S., A. Goldman, J.R. Gillis, R.R. Gamache, H.M. Pickett, R.L. Poynter, N. Husson, and A. Chedin, "AFGL Trace Gas Compilation: 1982 Version," *Appl. Opt.*, **22**: 1616, 1983a.
- Rothman, L.S., R.R. Germache, A. Barbe, A. Goldman, J.R. Gillis, L.R. Brown, R.A. Toth, J.-M. Flaud, and C. Camy-Peyret, "AFGL Atmospheric Absorption Line Parameters Compilation: 1982 Edition," *Appl. Opt.*, **22**: 2247, 1983b.
- Selby, J.E.A., F.X. Kneizys, J.H. Chetwynd, Jr., and R.A. McClatchey, "Atmospheric Transmittance/Radiance: Computer Code LOWTRAN 4," AFGL TR-78-0053, ADA058643, 1978.
- Sharma, R.D., "Near-Resonant Vibrational Energy Transfer Among Isotopes of CO₂," *Phys. Res.*, **177**: 102, 1969.
- Sharma, R.D., and C.A. Brau, "Energy Transfer in Near-Resonant Molecular Collisions due to Long-Range Forces with Application to Transfer of Vibrational Energy from ν₃ Mode of CO₂ to N₂," *J. Chem. Phys.*, **50**: 924, 1969.
- Sharma, R.D. and R.M. Nadile, "Carbon Dioxide (ν₂) Radiance Results Using a New Nonequilibrium Model," AIAA Reprint 81-0426, Aerospace Sciences Meeting, 1981.
- Sharma, R.D., R.M. Nadile, A.T. Stair Jr., and W. Gallery, "Earthlimb Emission Analysis of Spectral Infrared Rocket Experiment (SPIRE) Data at 2.7 μm Micrometers," *SPIE*, **304**: 139, 1981.
- Stair, A.T., Jr., J.C. Ulwick, D.J. Baker, C.L. Wyatt, and K.D. Baker, "Altitude Profiles of Infrared Radiance of O₃ (9.6 μm) and CO₂ (15 μm)," *Geophys. Res. Lett.*, **1**: 117, 1974.
- Stair, A.T. Jr., J.C. Ulwick, K.D. Baker, and D.J. Baker, "Rocketborne Observations of Atmospheric Infrared Emissions in the Auroral Region," in *Atmosphere of Earth and the Planets*, edited by B.M. McCormac, D. Reidel, Dordrecht, Holland, p. 335-346, 1975.

INFRARED AIRGLOW

- Stair, A.T. Jr., R.M. Nadile, J.C. Ulwick, K.D. Baker, and D.J. Baker, "Infrared Measurements of Auroral, Airglow and the Upper Atmosphere," AIAA Reprint 81-0421, Aerospace Sciences Meeting, Jan 1981.
- Stair, A.T. Jr., R.D. Sharma, R.M. Nadile, D.J. Baker, and W.F. Grieder, "Observations of Limb Radiance with Cryogenic Spectral Infrared Rocket Experiment (SPIRE)," *J. Geophys. Res.*, In Press, 1985.

- Taylor, R.L., "Energy Transfer Processes in the Stratosphere," *Can. J. Chem.*, **52**: 1436-1451, 1974.
- Ulwick, J.C., K.D. Baker, A.T. Stair Jr., W. Frings, R. Hennig, K.V. Grossman, and E.R. Hegblom, "Rocketborne Measurements of Atmospheric Infrared Fluxes," *J. Atmos. Terr. Phys.*, In Press, 1985.
- Zachor, A.S., R.D. Sharma, R.M. Nadile, and A.T. Stair Jr., "Inversion of SPIRE NO Data," AFGL TR-81-0325, ADA108866, 1981.